Design of bimetallic nanoparticles

Sung June Cho*

National Research Laboratory for Clean Energy Technology,
Department of Applied Chemical Engineering,
Chonnam National University,
Yongbong 300, Bukgu, Gwangju 500 757, Korea
E-mail: sjcho@chonnam.ac.kr
*Corresponding author

Ryong Ryoo

Department of Chemistry,
Korea Advanced Institute of Science and Technology,
Taeduk Science Town, Taejon 305 701, Korea
E-mail: rryoo@kaist.ac.kr

Abstract: A novel preparation method to control a microstructure and the resulting structure and activity relationship are presented to aim a rational design of the well defined bimetallic nanoparticles. Nanoparticles are engineered inside the supercage of faujasite type zeolite. The reduction mechanism for the bimetallic nanoparticles is proposed based on the results of X-ray absorption fine structure, ^{129}Xe NMR spectrum and transmission electron micrograph. The chemical properties have been modified and also the catalytic performance has been altered through the generation of well defined bimetallic nanoparticles. The principle of the design of bimetallic nanoparticles has also been extended for other open substrates. The *state of the art* technology for the fabrication method presented here provides advanced firm basis for the development of the bimetallic nanoparticles with novel function.

Keywords: bimetallic nanoparticles; XAFS; ^{129}Xe NMR; catalysis; reduction mechanism; microstructure.

Reference to this paper should be made as follows: Cho, S.J. and Ryoo, R. (2006) 'Design of bimetallic nanoparticles', *Int. J. Nanotechnology*, Vol. 3, Nos. 2/3, pp.194–215.

Biographical notes: Sung June Cho received a BSc in Physical Chemistry in 1992 and a PhD in Physical Chemistry on bimetallic nanoparticles supported on faujasite type zeolite from Korea Advanced Institute of Science and Technology in 1997. Thereafter, he joined Korea Institute of Energy Research as a senior scientist for the development of high temperature catalytic combustion catalyst. He developed a new method for the synthesis of hexaaluminates, high temperature combustion catalyst, and the PtPd bimetallic nanoparticles supported Cordierite for gas turbine power generation. He has (co-) authored over 50 publications and technical reports, presented 20 invited lectures at universities and research institutes, 10 talks in at major international conferences worldwide. He is presently an assistant professor at the Department of Applied Chemical Engineering, Chonnam National University, Gwangju, Korea since 2002. His laboratory was selected as National Research Laboratory in fields of clean energy technology in 2002.

Ryong Ryoo received his BS degree from Seoul National University in 1977 and PhD degree on heterogeneous catalysis (Advisor: Professor Michel Boudart) from Department of Chemistry, at Stanford University in 1985. He was a Postdoctor in Professor Alex Pines's Laboratory for solid state NMR at University of California at Berkeley in 1985. He joined Korea Advanced Institute of Science and Technology in 1986 as a Faculty member. He is now a full professor in Department of Chemistry at KAIST and the director of National Creative Research Initiative Center for Functional Nanomaterial funded by: Korea Science & Engineering Foundation. His research area is chemistry of advanced materials. Current research topics in the laboratory are focused on synthesis, characterisation and applications of nano-structured materials such as mesoporous molecular sieves, metal nanowires and metal clusters. He got numerous awards; Best Paper Award: Korean Chemical Society, 2000, Best Paper Award: Korean Federation of Science and Technology Societies, 2001, Research of Future Award: ACS, 2001, Scientist of the Month Award: Korea Science & Engineering Foundation, 2001, Best Paper Award: *Journal of Electron Microscopy*, 2001, Professor of the Year Award: KAIST, 2001, Grand Prize for Academic Achievement: Korean Chemical Society, 2002, The Supreme Scientist of Korea Award, Ministry of Science and Technology, 2005. He has (co) authored more than 150 publications has been an invited and plenary lecturer in numerous international conferences.

1 Introduction

Nanoparticles of novel metals have attracted much attention due to unique catalytic performance in various reactions [1]. The nanoparticle can be classified as a zero dimensional entity. The electrochemical, magnetic and optical properties of these nanoparticles are totally different from those of bulk metals. Preparation of such a nanoparticle has been investigated since 1970 [2]. There are many different methods for the preparation of nanoparticles, ion exchange, impregnation, chemical vapour deposition, etc. Traditional methods such as ion exchange and impregnation are still routines for the preparation of industrial catalysts. Microstructure of the obtained nanoparticles has been studied with gas adsorption, X-ray diffraction and transmission electron microscopy [3–5]. However, there was little information available about the number of atoms per nanoparticles and the surface structure.

Extended X-ray absorption fine structure (XAFS) has been used to characterise the local atomic structure in nanomaterials. Sinfelt and coworker applied it to find out the structure of bimetallic nanoparticle catalyst used in catalytic conversion of hydrocarbon [6]. The bimetallic nanoparticles were prepared with the incipient impregnation method of both metal salts on alumina. In 1990, Ichikuni and Iwasawa investigated the polymer supported nanoparticles with XAFS [7]. They showed that uniform sized nanoparticles can be prepared by reduction in solution phase. The microstructure of the nanoparticle was simulated based on the XAFS results. Still, there was a lack of information on the surface structure of nanoparticles.

The microstructure of the nanoparticles depended on the sequence of the loading of metal salts and the choice of pretreatment methods. The control of the surface structure of bimetallic nanoparticles is essential in the current preparation technology [8]. A surface technique such as XPS is possible characterisation method for the surface

structure of the nanoparticles. However, the supported nanoparticles are dispersed on high surface area substrate, resulting in much difficulty in measurement and analysis. Thus, other effective method such as ^{129}Xe NMR spectroscopy is necessary for the characterisation of the surface structure. ^{129}Xe NMR spectroscopy was pioneered by Fraissard and coworkers in the 1980s [9–11]. The technique was used extensively to probe the micropore and surface structure of zeolite related materials. The presence of the nanoparticles inside the cage of microporous materials gives a rise in ^{129}Xe NMR chemical shift due to the strong interaction between Xe atoms and metal surface. The degree of the interaction depended much on the concentration and type of metal presented at the surface.

This review describes the design of bimetallic nanoparticles based on the investigation of monometallic nanoparticles. Through the rational design of the bimetallic nanoparticles, the electronic property and the catalytic activity can be controlled as expected. The examples included the PtSn and PtNi bimetallic nanoparticles supported on KL zeolite and PtPd bimetallic nanoparticles on thermally stable alumina. The knowledge on the design of the bimetallic nanoparticles has been built based on the investigation on the preparation and characterisation of monometallic nanoparticles such as, Pt [12], Ir [13], Rh [14], Ru [15] and Pd [16].

2 Theory and experimental

2.1 Preparation of monometallic nanoparticles and bimetallic nanoparticles

Monometallic nanoparticles can be prepared with three different methods after the impregnation and ion exchange into suitable supports. The calcinations-reduction treatment is suitable for the generation of Pt [12], Pd [16] and Rh [14] nanoparticles. The evacuation or thermal decomposition-reduction is suitable for the Ir [13] and Ru [15] nanoparticles. The direct reduction is preferred to prepare the sponge like metal aggregates such as Pt and Pd. Depending on the pretreatments, the location of metal particle can be altered and also the resulting adsorption and catalytic properties can be modified. If the Ir and Ru are subject to the oxidation or calcination, the significant particle growth or sintering was resulted due to the volatile metal oxide complex such as RuO_4(g) or RuO_3(g) [17,18]. Thereby, the gas adsorption and catalytic properties were deteriorated.

For the preparation of bimetallic nanoparticles, the pretreatment should be selected carefully since one metal can sinter and the other does not. Also, the order of the loading of metal salt is critical for the preparation of bimetallic nanoparticles. Figure 1 shows the imaginative bimetallic nanoparticle structures. The first one can considered just mixture of two independent monometallic nanoparticles. The second one is single phase alloy particles that can be obtained through simultaneous loading of the two types of metals. The last one is the bimetallic nanoparticle structure of cherry model. In this case, the other metal component can be supported subsequently on the substrate containing one metal component. The proper treatment can be selected to obtain such unique structure.

Figure 1 Schematics for the possible structure of the bimetallic nanoparticles

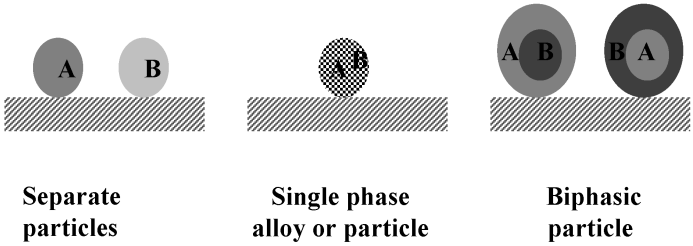

Figure 2 shows the transmission electron micrographs of the Pt nanoparticle supported on NaY zeolite. The Pt nanoparticles can be found in Figure 2(a). It was prepared with the calcination and the subsequent reduction by flowing hydrogen after the ion exchange of $Pt(NH_3)_4^{2+}$ into NaY zeolite. The estimated size was 1 nm, referred from the result of TEM, hydrogen chemisorption, Xe adsorption, and XAFS. The loading was controlled to 2 wt%. The Figure 2(b) showed the Pt nanoparticles after the ion exchange of additional $Pt(NH_3)_4^{2+}$ into NaY zeolite, 8 wt% and subsequent calcination-reductions. The particle size in Figure 2(b) was the same as that in Figure 2(a). It seems that the calcinations-reduction resulted in the formation of separate Pt nanoparticles after the additional loading of Pt complex. Table 1 shows the results of the xenon adsorption measurement and atomic structural parameters from XAFS. The results on the sample in Figure 2(a) and 2(b) indicated the same Pt nanoparticle size. Comparison with the results on 10 wt% Pt nanoparticle samples suggested that the calcination-reduction method led to the formation of separate nanoparticles after the second ion exchange [12].

Direct reduction of the second loaded Pt complex resulted in the formation large Pt metal particles. The xenon adsorption decreased to 0.018 and the atomic structural parameter indicated the bulk Pt. However, the particle size was limited to 3–4 nm. The formation mechanism can be modelled as in Figure 3. Initially, 2 wt% Pt sample contained 1 nm size Pt nanoparticles entrapped in NaY zeolite supercage. The additional loading of the Pt complex can result in either 1 nm Pt nanoparticle through the calcinations-reduction or 3–4 nm Pt nanoparticle through the direct reduction. It can be assumed that the preloaded Pt nanoparticle can be reduced readily through the contact with hydrogen even at room temperature. Thus, the highly reducing agent, atomic hydrogen was present on the surface of the preloaded nanoparticle. The secondly loaded Pt complex can be reduced near or at the surface of the preloaded nanoparticle by the adsorbed atomic hydrogen [8]. This reduction mechanism is proposed in Figure 4.

Figure 2 Transmission electron micrograph of Pt cluster supported on Y zeolite: (a) Pt/NaY obtained through the calcination and the subsequent reduction; (b) $Pt(NH_3)_4^{2+}$ was exchanged into Pt/NaY, treated in flowing oxygen at 593 K and subsequently reduced at 573 K and (c) $Pt(NH_3)_4^{2+}$ was exchanged into Pt/NaY and subsequently reduced with hydrogen at 573 K

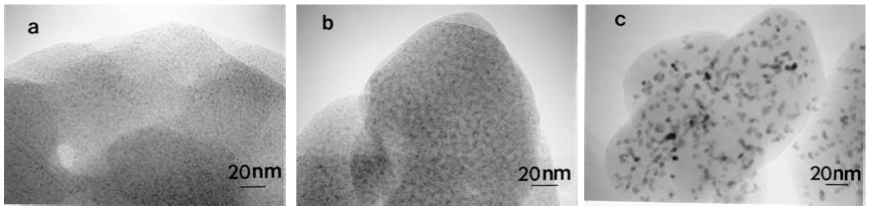

Table 1 Results of the characterisation with xenon adsorption measurement and XAFS

Sample	*Xe/Pt*	n^a	CN^b	R (nm)^c
2 wt% Pt/NaY[e]	0.069	58	5.0	0.275
2 + 8 wt% Pt/NaY(CR)[f]	0.083	55	5.4	0.276
10 wt% Pt/NaY[e]	0.066	61	5.1	0.276
2 + 8 wt% Pt/NaY(DR)[g]	0.018	–	12.0	0.277

[a]Average number of atoms per Pt particle calculated following the method presented in the reference [12].

[b]Pt-Pt coordination number (±0.5)

[c]Pt-Pt distance (±0.001)

[e]The samples were prepared through the calcinations-reduction.

[f]The sample was prepared through the calcinations-reduction after the second ion exchange of additional Pt complex.

[g]The sample was prepared through the direct reduction after the second ion exchange of additional Pt complex.

Figure 3 Schematics for the structural model for the formation of nanoparticles through the different preparation method

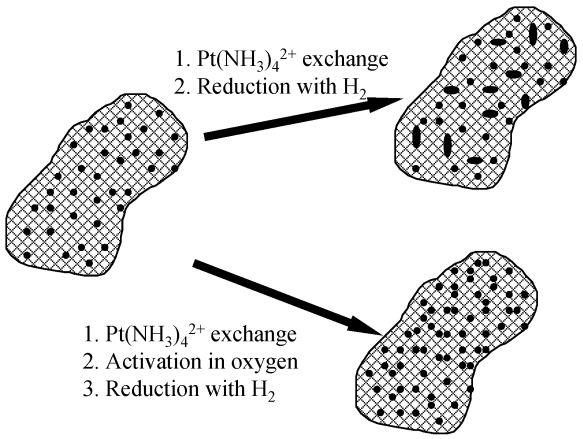

Figure 4 Schematics for the reduction mechanism. The Pt nanoparticle was preloaded and subsequently M^{n+} is loaded secondly

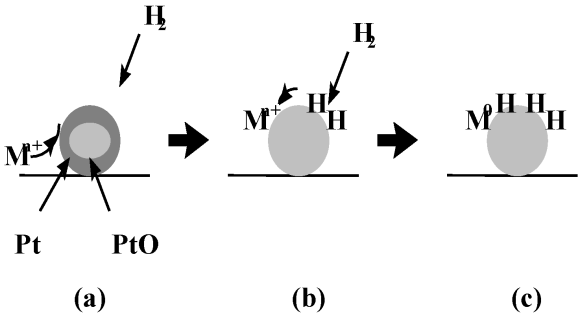

The reduction mechanism for the bimetallic nanoparticles was tested for the PtPd nanoparticles supported on NaY zeolite [8,19]. In Table 2, Pt nanoparticle was prepared first and Pd was loaded secondly. Depending on the preparation methods, it was found that the same trend in the results of the xenon adsorption measurement and oxygen chemisorption as that of Pt nanoparticle above-mentioned. The Xe/M of the Pd/Pt/NaY (DR) was 0.076 when only the Pt content was considered. It meant that the preloaded Pt play a role as a seed for the reduction and formation of Pd nanoparticle over the Pt nanoparticle. This result suggested that the reduction mechanism outlined in Figure 4 can be applied to the preparation of well-defined nanoparticles.

Table 2 Results of the characterisation with xenon adsorption measurement and oxygen chemisorption*

Sample	*Xe/M*[a]	*O/M*[b]
Pt/NaY (CR)	0.081	0.73
Pd/Pt/NaY(DR)	0.015 (0.076)[c]	0.13 (0.74)[c]
Pd/Pt/NaY(CR)	0.094	0.62
Pd/NaY(DR)	–	–

[a]From xenon adsorption method and M includes Pt and Pd.

[b]Total oxygen chemisorption and M includes Pt and Pd.

[c]Only the Pt content is considered.

*CR and DR indicated the calcinations-reduction and the direct reduction, respectively.

In this review, the preloaded Pt nanoparticle and Pd nanoparticle were representative as seed for the loading of other metals such Sn and Ni. The pretreatment condition adopted in this work was direct reduction since it aimed to cover the preloaded Pt nanoparticle with the secondly loaded metal, resulting in the cherry model structure as illustrated in Figure 1.

Experimental procedures for the preparation of Pt nanoparticle on KL zeolite (Pt/KL) are described earlier [20]. Briefly, a large batch of 2 wt% Pt/KL, ~5 g, was obtained from the activation in O_2 at 593 K for 2 h and the subsequent reduction with H_2 at 573 K for 2 h after the ion exchange of $Pt(NH_3)_4^{2+}$ into KL zeolite (ELZ-L, Union Carbide, $K_9[(AlO_2)_9(SiO_2)_{27}]$).

Sn^{2+} was exchanged at room temperature onto the 2.0 wt% Pt/KL sample at a low pH and under dilute condition to avoid the formation of SnO or SnO_2 precipitates. The ion exchanged zeolite was filtered, washed with doubly distilled water, dried in a vacuum oven at room temperature, and subsequently placed on a fritted disk inside a Pyrex U-tube flow reactor. The zeolite was reduced with heating in H_2 flow (99.999%, passed through a MnO/SiO_2 trap). The H_2 flow rate for the reduction was 200 mL min^{-1} g^{-1}, and the reduction temperature was linearly increased from room temperature to 573 K over 4 h and maintained at 573 K for 2 h. The incorporation of nickel and palladium onto the Pt cluster was performed in the same way as above. The average number of metal atoms per Pt cluster was controlled to 1 and 2. The resulting samples are designated as the SnPt/KL and the NiPt/KL.

For the preparation of PtPd nanoparticles on alumina, $Pd(NO_3)_2$ (Engelhard, 19.9% Pd) was impregnated into La-doped Al_2O_3 (2 mol% La-Al_2O_3) supplied from Condea Inc. Its surface area was 90 m^2 g^{-1}. The activation procedure was the calcination in oxygen at

823 K for 6 hr followed by the reduction with hydrogen at 823 K for 4 h. The Pd loading of the catalyst was 2 wt% on dry basis. The obtained Pd catalyst was denoted as Pd/La-Al_2O_3.

The bimetallisation by platinum was performed as follows: the reduced Pd nanoparticle was impregnated with the aqueous solution containing the desired amount of H_2PtCl_6. The platinum complex impregnated Pd catalyst was dried in oven at 373 K for overnight. The obtained sample was reduced up to 823 K by flowing hydrogen without the activation in oxygen flow. The platinum loading, the Pt/Pd ratio was controlled to 0, 0.5, 1.0 and 2.0, respectively. The bimetallic nanoparticle catalyst was also denoted as Pt/Pd/La-Al_2O_3.

2.2 Characterisation and catalysis

Natural xenon gas (Matheson, 99.995%) was used for adsorption measurement as well as ^{129}Xe NMR experiment. Xenon and hydrogen adsorption measurements were performed at 296 K with a conventional volumetric gas adsorption apparatus. The adsorption temperature was controlled to within 296 ± 0.1 K by a constant-temperature circulation bath.

Hydrogen chemisorption at 296 K was measured volumetrically after the pre-adsorbed hydrogen atoms were desorbed at 673 K in vacuum (1×10^{-3} Pa) for 2 h and the sample cooled to 296 K. Extrapolation of this adsorption isotherm from 13–53 kPa to zero pressure was referred to as total hydrogen chemisorption value, H_{total}/Pt_{total}. The sample was then evacuated at 296 K for 2 h and a second isotherm was measured, which corresponded reversible hydrogen chemisorption value, H_{rev}/Pt_{rev}.

For ^{129}Xe NMR experiment, a special ^{129}Xe NMR tube equipped with high vacuum stopcocks was joined to the above U-tube reactor by glass blowing before powder sample was placed into the reactor. After the sample was reduced and evacuated, a 0.5 g portion was transferred from the reactor to the NMR tube by tilting the reactor and then sealed with flame. Xenon gas was equilibrated with the sample to a desired pressure at 296 K through the vacuum stopcocks. ^{129}Xe NMR spectra were obtained from the adsorbed gas at 296 K with a Bruker AM 300 instrument operating at 83.0 MHz for ^{129}Xe with a 0.5-s relaxation delay. The chemical shift is referenced to xenon gas extrapolated to zero pressure.

X-ray absorption fine structure (XAFS) for the samples were obtained with self-supporting wafers of 10 mm in diameter pressed with 0.20 g powder sample. Since the sample wafers were exposed to air during the wafer pressing, each wafer was reduced again with H_2 flow at 573 K inside a Pyrex U-tube flow reactor and evacuated at 673 K to remove the chemisorbed hydrogen. The sample wafer was then moved to a joining XAFS cell, similar to ^{129}Xe NMR experiment. The XAFS cell was fabricated with Pyrex glass and Kapton windows (Du Pont, 125 μm thick). The Kapton windows were joined using Torr Seal (Varian). The XAFS cell containing sample wafer under He gas was sealed with flame and stored in a vacuum desiccator until XAFS measurement.

The XAFS in He gas was measured at the Pt L_{III} edge at room temperature using Beam Line 10B at the Photon Factory in Tsukuba and also at the Beam Line 3C1 at the Pohang Accelerator Laboratory, Korea. The ring current was maintained at 300–350 mA during the measurements. A Si(311) channel cut monochromator was used. The X-ray energies for X-ray absorption near edge structure (XANES) and EXAFS at the Pt L_{III} edge were increased by 0.5 eV and 1.9 eV, respectively. The X-ray intensity was

measured by using a gas ionisation chamber. The detector gases for I_0 and I were 100% Ar and 100% Kr, respectively.

XAFS for the SnPt/KL and the NiPt/KL were obtained above the Pt L_{III} edge. The XAFS data in the wave vector (k) range between 30 and 140 nm^{-1} were analysed using UWXAFS2 program package [21]. The EXAFS oscillation ($\chi(k)$) was multiplied by the wave vector cube (k^3) after background removal and normalisation. Background was removed with a r-space technique in which low-r background components in the Fourier transform (FT) are optimised through the comparison with a standard XAFS generated using FEFF5 code [22]. Fourier transformation were performed from $30 \le k \le 140$ nm^{-1} to $0.18 \le r \le 0.30$ nm using Hanning window function. The curve fitting for the EXAFS was performed without Fourier filtering. The number of parameters used in the curve fitting was less than the allowed maximum number of parameters, $N_{free} = 2/\pi \cdot \delta r \cdot \delta k + 2$, where δk is the FT range in k-space, and δr is the fitting range in r-space.

The rate of catalytic conversion of *n*-hexane to benzene was measured with typically 20 mg catalyst using a Pyrex batch recirculation rig similar to the one described by Schlatter and Boudart [23]. The reactant gas consisted of *n*-hexane, H_2 and He with partial pressures of 6, 36 and 59 kPa, respectively. *n*-Hexane (Merck, HPLC grade) was used after purification through three freeze-evacuation-thaw cycles. The total volume of the rig was 620 mL. The gas recirculation rate was 4.0 L min^{-1}. The reaction temperature was controlled to 671 ± 1 K. Products were analysed with a gas chromatograph (GC, HP 5890 Series II) equipped with a Carbowax 20M column using a flame ionisation detector.

The catalytic activity of benzene hydrogenation was measured in a similar way for *n*-hexane aromatisation. The reactant gas consisted of benzene, H_2 and He with partial pressures of 4, 41 and 63 kPa, respectively. Benzene (J.T. Baker, Baker analysed) was used after purification through three freeze-evacuation-thaw cycles. The reaction temperature was controlled to 423 – 523 ± 0.1 K. The total number of benzene converted per metal was defined as the turnover number (N_t), based on the total number of metal atoms. The catalytic activity of different samples was reported as an average turnover frequency (υ_t) taken in the same N_t range of 10–50.

The catalytic activity of methane combustion over the sample was measured using the microreactor system equipped with gas chromatograph (HP5890, Hewlett Packard). The methane concentration was controlled to 1 vol% and 99% air. The space velocity, GHSV was 30,000 h^{-1}.

3 Result and discussion

3.1 MPt/KL catalyst

PtSn bimetallic nanoparticles have drawn much attention due to a high resistance to coke deposition during naphtha reforming [24,25]. Incorporation of tin into Pt nanoparticles and bulk Pt surface is known to lead to a formation of PtSn nanoparticles and Sn/Pt surface alloy, respectively. Meriaudeau et al. [26] prepared the PtSn nanoparticles on NaY zeolite by contacting Pt surface covered with hydrogen with tetramethyltin compound, thereby reacting the alkyltin compound with Pt surface. For Sn/Pt(111) surface alloy, Xu et al. [27] found the substantial electronic effect by tin incorporation on adsorption-desorption kinetics of cyclohexane and benzene. Cortright and Dumesic [28]

obtained PtSn nanoparticles inside KL zeolite channel by reduction with H_2 at 773 K after the impregnation of tributyltin acetate onto the zeolite followed by a second impregnation of $Pt(NH_3)_4(NO_3)_2$. The catalysts showed a high activity and selectivity of isobutane dehydrogenation, which was attributed to the reduced Pt ensemble size by tin and potassium, and zeolite pore structure.

The previous studies on Pt/KL catalyst showed that Pt nanoparticles containing 5–7 atoms on the average can be prepared independent of Pt content up to 5.2 wt% without a pore blockage for xenon adsorption [20]. Figure 5 shows xenon adsorption isotherms on the PtSn/KL catalysts at 296 K. Amount of xenon adsorption per unit cell for the PtSn/KL catalysts was the same as that of KL zeolite, indicating no pore blockage for xenon adsorption upon the incorporation of tin. The incorporation of tin into the Pt/KL catalyst seems not to cause the growth of particle size in the PtSn/KL catalyst.

Figure 5 Xenon adsorption isotherms of the SnPt/KL catalysts with an atomic ratio of 0.0 (O), 0.1 (□), 0.2 (Δ) and 0.4 (∇) obtained at 296 K

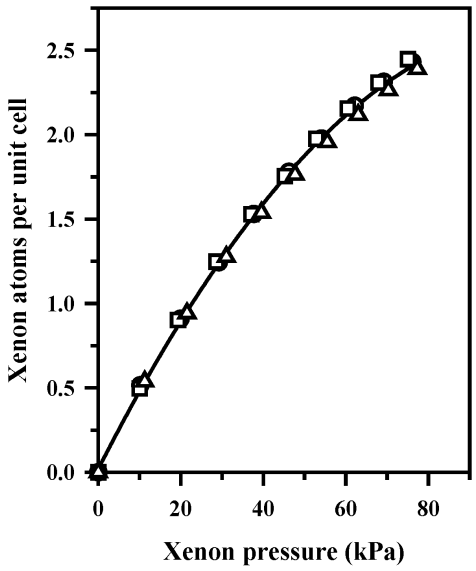

Results of hydrogen adsorption on the PtSn/KL catalysts are presented in Table 3. The amount of total hydrogen adsorption on the PtSn/KL catalysts decreased too much, compared to that of the Pt/KL catalyst. Further, all the adsorption became reversible. Therefore, tin seems to cover the hydrogen adsorption site of Pt nanoparticle blocking a strong adsorption of hydrogen. The complete removal of adsorbed hydrogen at room temperature made it difficult to measure the amount of xenon adsorption only on Pt nanoparticles that can be obtained from the difference between two xenon adsorption isotherms before and after hydrogen chemisorption. It was believed that unique gas adsorption characteristics come from the interaction Sn and Pt nanoparticles.

^{129}Xe NMR spectra of xenon adsorbed on the PtSn/KL catalysts are shown in Figure 6. The chemical shift of xenon adsorbed on the PtSn nanoparticles decreased from 137 ppm to 123 ppm upon tin incorporation. The chemical shift of the PtSn/KL catalyst with an atomic ratio of 0.4 was similar to that of the Pt/KL catalyst with chemisorbed hydrogen. According to the previous reports, the interaction of xenon with the

Pt nanoparticles can be inhibited due to the increase of surface coverage by metals such as Ag [29] and Cu [30], since these metals have no interaction with xenon. Thus, the decrease of the chemical shift for the PtSn/KL catalyst was consistent with the coverage of Sn on Pt nanoparticles if Sn plays a same role as Ag and Cu.

Table 3 Hydrogen chemisorption and xenon adsorption on the SnPt/KL catalysts

Sn/Pt	H_{total}/Pt_{total} [a]	H_{rev}/Pt_{rev} [b]	Xe/Pt_{total} [c]
0.0	1.6	0.5	0.20
0.1	1.0	1.0	~0
0.2	0.6	0.6	~0
0.4	0.6	0.6	~0

[a]Total hydrogen chemisorption at 296 K, based on the total amount of Pt.

[b]Reversible hydrogen chemisorption at 296 K, based on the total amount of Pt.

[c]Xenon adsorption on the PtSn nanoparticles at the saturation obtained from the difference between two xenon adsorption isotherms with and without chemisorbed hydrogen based on the total amount of Pt.

Figure 6 ^{129}Xe NMR spectra of xenon adsorbed on the SnPt/KL catalysts at 296 K and under 53.3 kPa: (a), KL zeolite; (b), 2 wt% Pt/KL; the SnPt/KL with an atomic ratio of (c) 0.1, (d) 0.2 and (e) 0.4

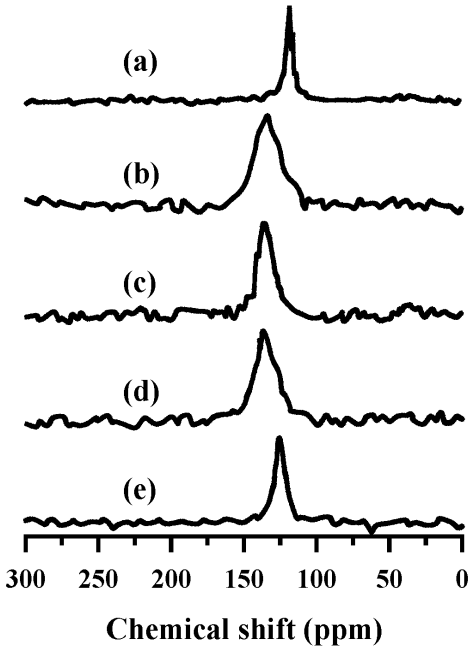

Figure 7 showed the ^{129}Xe chemical shift change as a function of the pressure with the increase of Ni content in the Ni/Pt/KL catalysts. The chemical shift of the xenon adsorbed on the Ni/Pt/KL catalyst decreased initially with the decrease of the pressure and increased at low pressure below 20 kPa due to the contribution of the interaction between xenon and nickel metals. The interaction between xenon and platinum metal

resulted in the chemical shift about 1300 ppm when extrapolated to zero pressure [12]. Similarly, the interaction between xenon and palladium metal give a chemical shift change about 3000 ppm [16]. This trend suggests the interaction between xenon and nickel may result in the more than 3000 ppm chemical shift change. Thus, the chemical shift change was increased too much with the increase of nickel content. And also, the fact that the chemical shift is mostly due to the direct surface interaction indicated that the secondly loaded nickel located at the surface of Pt nanoparticles as illustrated in Figure 8.

Figure 7 ^{129}Xe NMR chemical shift of xenon adsorbed on the NiPt/KL catalysts as function of xenon pressure at 296 K: (○) 2 wt% Pt/KL, (□) NiPt/KL (Ni/Pt = 0.1), (△) NiPt/KL (Ni/Pt = 0.2) and (□) NiPt/KL (Ni/Pt = 0.4)

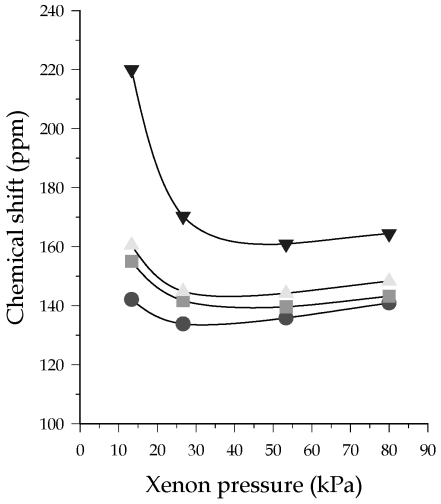

Figure 8 Schematics for the interaction between xenon and NiPt bimetallic nanoparticles

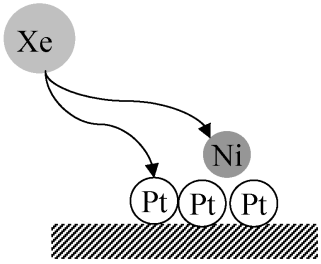

XAFS spectra for the SnPt/KL and NiPt/KL catalysts were obtained above the Pt L_{III} edge and analysed with the UWXAFS2 and FEFF5 [21,22]. The structural parameters obtained through the curve fitting are listed in Table 4. The Pt-Pt coordination number (CN) in the SnPt/KL and NiPt/KL catalysts did not change significantly upon the incorporation of tin and nickel. This result of CN meant that there was no increase of the particle size. The Pt-Pt distance increased to 0.268 nm from 0.258 nm for the SnPt/KL catalysts like a structural relaxation by hydrogen adsorption on Pt nanoparticles [20]. The results of XAFS experiment suggested that the incorporation of Sn or Ni into Pt nanoparticles could not cause an increase of particle size, in agreement with the

results of xenon adsorption. The chemical state of Sn or Ni in the SnPt/KL catalyst found to be Sn^{2+} referred from the obtained Pt-Sn distance while the Ni was reduced, referred from the distance of Ni-Pt, 0.251 nm.

Table 4 Structural parameters obtained from the XAFS curve fitting of Pt L_{III} XAFS of the SnPt/KL and NiPt/KL catalyst

	Pair	*CN*[a]	*R* (nm)[b]	σ^2 (pm^2)[c]
		Pt/KL		
	Pt-Pt	3.3	0.258	79
	Pt-O	3.5	0.256	584
		SnPt/KL		
Sn[d]	Pt-Pt	4.7	0.268	70
	Pt-Sn	0.5	0.280	28
		NiPt/KL		
Ni[d]	Pt-Pt	3.2	0.263	73
	Pt-Ni	0.8	0.251	104

[a]Coordination number.

[b]Bond distance.

[c]The Debye-Waller factor.

[d]Sample in He with M/Pt = 0.2.

n-Hexane aromatisation over the SnPt/KL catalysts was performed at 671 K with $H_2/C_6H_{14} = 6$. Turnover frequency (υ_t) based on the amount of total Pt decreased progressively with the increase of Sn content near 10% conversion level of *n*-hexane aromatisation as shown in Figure 9. The decrease of catalytic activity for *n*-hexane aromatisation seems probably due to the surface coverage of Sn over Pt nanoparticles in the SnPt/KL catalyst. The product distribution of *n*-hexane aromatisation is also illustrated in Figure 10. The reaction data were consistent with that the incorporation of Sn onto the Pt nanoparticles suppress an isomerisation to hexanes and 1,5-ring formation to methylcyclopentane, resulting in an increased selectivity to benzene from 50% to 80% with the Sn content. The content of potassium in the SnPt/KL catalyst was controlled to $8.49 \sim 8.29\ K^+$ ion depending on the content of tin. The effect of such a small change of alkali loading in the KL zeolite seems to be negligible under the reaction condition. The reaction data under the similar alkali loading, combined with the result of characterisation data suggested that the decrease of Pt ensemble size by tin can suppress the formation of highly dehydrogenated species required for hydrogenolysis, isomerisation and coke deposition, resulting in the high selectivity to benzene.

Benzene hydrogenation has usually been classified as structure insensitive [31] but it seems to be very risky because some catalysts show the dependence of the catalytic activity on the metal particle size. The catalytic activity of benzene hydrogenation over Pt/SiO_2 is reported ten times higher than Ni/SiO_2 under the similar condition as shown in Table 5 [32]. It can thus be expected that the incorporation of nickel onto the Pt nanoparticles leads to the significant decrease of the catalytic activity in benzene hydrogenation. However, an increase of the amount of nickel in the NiPt/KL decreased

the activity decently and accelerated the reaction to the formation of cyclohexane, indicating an alloy effect.

Figure 9 The catalytic activity of *n*-hexane aromatisation over the SnPt/KL catalysts plotted against the atomic ratio of Sn/Pt. The reaction was performed at 671 ± 1 K with $H_2/C_6H_{14} = 6$. υ_t was based on the total amount of Pt

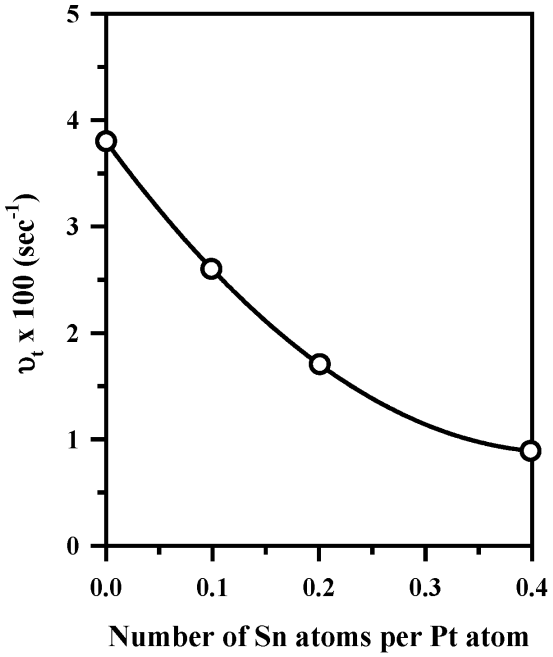

Figure 10 The product selectivity of *n*-hexane aromatisation over the SnPt/KL catalysts

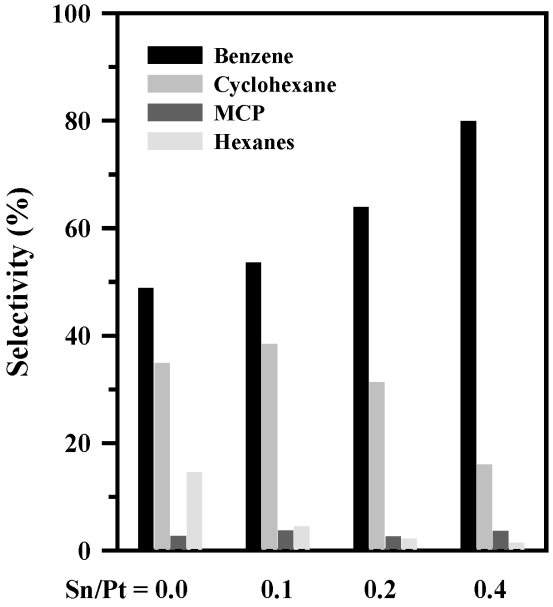

Table 5 Catalytic activity of the NiPt/KL catalysts over benzene hydrogenation and their apparent activation energy

n^a	υ_t (sec^{-1})^b	E_a (kJ mol^{-1})^c
0	0.067	41
1	0.022	60
2	0.076	62

[a]Average number of the incorporating nickel atoms per Pt nanoparticle.

[b]Turnover frequency based on total number of atoms.

[c]Apparent activation energy was obtained from the Arrhenius plot in the temperature range in which the catalytic activity increased.

Concerning the deactivation behaviour, the catalytic activity did not decrease at all during the second reaction when one nickel atom per Pt nanoparticle incorporated. However, the deactivation in other samples occurred during the repeated reactions. Primary source of deactivation is known to be a coke formation such as cyclohexylbenzene and dicyclohexylbenzene [33]. The resistance to the deactivation in the NiPt/KL seems due to the formation of NiPt bimetallic particle. The change of apparent activation energy and the temperature of maximum benzene hydrogenation over the NiPt/KL catalyst may suggest the presence of different electronic structure, which is responsible for the adsorption-desorption kinetics of benzene.

3.2 Pt/Pd/La-Al_2O_3 catalyst

In the previous work, we suggested the reversible structural model of the Pd catalyst during the thermal cycling as shown in Figure 11 [8,34]. The PdO seems to convert to the surface attached PdO state at 950 K after the desorption of oxygen upon increasing the temperature. Rodriguez et al. [35] proposed the PdAlOx as the surface attached PdO species. The surface attached PdO species was further reduced to Pd metallic state at 1023–1073 K that is susceptible for the particle growth upon the excessive heating, thereby losing the catalytic activity.

Figure 11 The reversible structural transformation in Pd catalyst

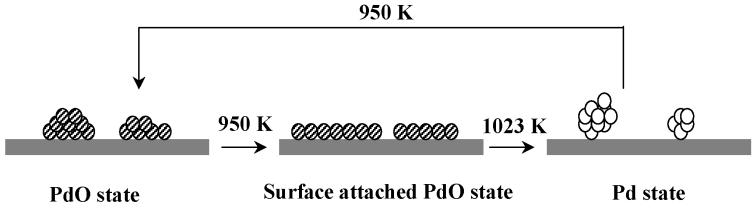

The thermal stabilisation of the Pd catalyst was also investigated using the surface coating of titanium oxide that is known to have the strong metal support interaction [36]. The near edge spectra of PdO and Pd foil is presented in Figure 12 to illustrate the difference of the near edge structure above the Pd K edge. The X-ray absorption at the Pd K edge in Pd foil was suppressed due to the dipole forbidden transition. The intensity of the $4s \rightarrow dp$ transition and the presence of $4s \rightarrow dsp$, dp can be traced in order to clarify the atomic and electronic change upon the heating. In the XANES experiment, the

transformation temperature from PdO to Pd was increased by the surface coating while the reverse transformation occurred at the similar temperature. This characteristic change of the metal oxide surface coated Pd catalyst is also shown in Figure 13. The sudden change of near edge spectra occurred at above 1123 K, which corresponded to the transformation of PdO to Pd. While, the reverse transformation from Pd to PdO occurred at 973 K. Such a transformation behaviour is the same as that of Pd catalyst, except the high transformation temperature from PdO to Pd by 100 K. Thus, the thermal stability can be improved by the coating of metal oxides onto the Pd catalyst.

Figure 12 Neat edge spectra of the (a) Pd foil and (b) PdO. The absorption inflection corresponds to $4s \rightarrow d$ and the second and third peaks correspond to *dp* and *dsp* transitions, respectively

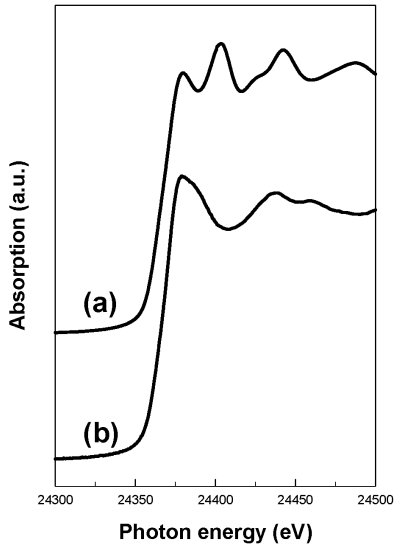

Figure 13 Near edge spectra of the metal oxide surface coated Pd catalyst measured as a function of heating temperature. (The inserted bars are the guides for the change of the edge features)

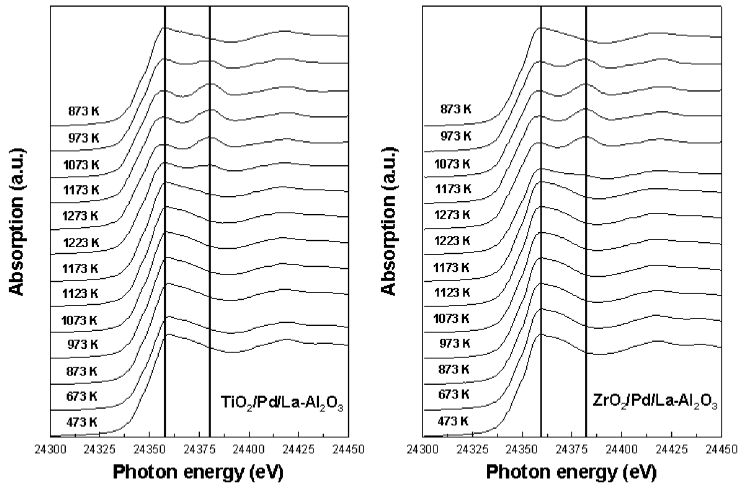

Further, the drastic change in the near edge spectra occurred in the bimetallised Pd nanoparticle by Pt as shown in Figure 14. Upon the increase of the Pt content, the near edge structure changed progressively to resemble to that of Pd foil. At the high loading of Pt, the XANES spectrum was almost the same as that of Pd foil. The model for the formation mechanism of bimetallic nanoparticles was proposed using the Pt nanoparticle in zeolite cage [12]. The preloaded Pd catalyst is easy to reduce upon heating in hydrogen flow at low temperature, ~373 K. During the reduction of the secondly loaded platinum complex without the activation in oxygen, the reduced preloaded palladium metal nanoparticles adsorb atomic hydrogen and the platinum complex ion moves the site of palladium nanoparticles to be reduced readily. Such a mechanism also resulted in the formation of the *M* surface-enriched Pd particle as illustrated in Figure 15. Thus, the palladium metal covered with platinum has no contact with oxygen or oxygen coordination when increasing Pt content [8]. The results of the data analysis of the XAFS spectrum of the bimetallised Pd catalyst are shown in Tables 6 and 7. At the Pd K edge, the oxygen coordination around the palladium atom disappeared as the increase of platinum content. The overall coordination number was 9 ± 1 with 0.270 nm of metal distances, indicating the reduced metallic state in the bimetallic nanoparticles. The particle size estimated from the coordination number was 1–2 nm. The oxygen coordination, however, was detected at the Pt L_{III} edge in the series of the bimetallised catalysts. The coordination number of bimetallic pair decreased progressively with the increase of the platinum content. The total metallic coordination number was 6 ± 1 with 0.271 nm of metal distances, consistent with the formation of the nanosized particles.

Figure 14 Near edge spectra of the bimetallic PtPd nanoparticle supported on alumina measured as a function of Pt/Pd ratio

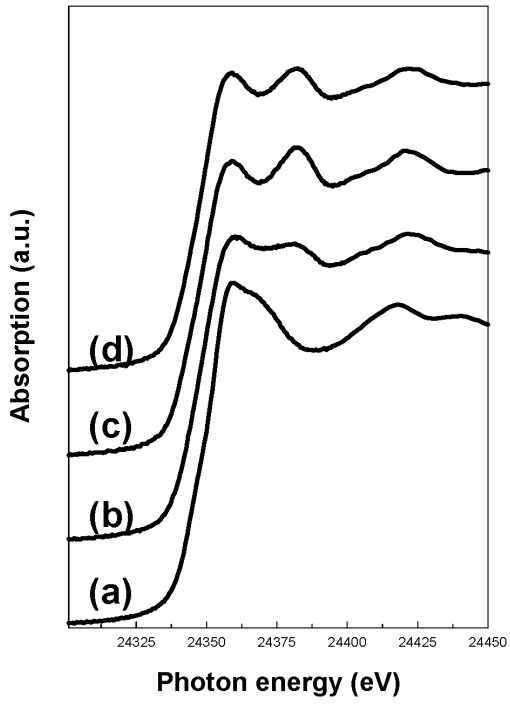

Figure 15 Schematic of the reduction mechanism: (a) the reduction of the preloaded Pd nanoparticle, (b) the formation of adsorbed atomic hydrogen and the subsequent reduction of the secondly loaded metal ion, and (c) the formation of M surface-enriched Pd particle

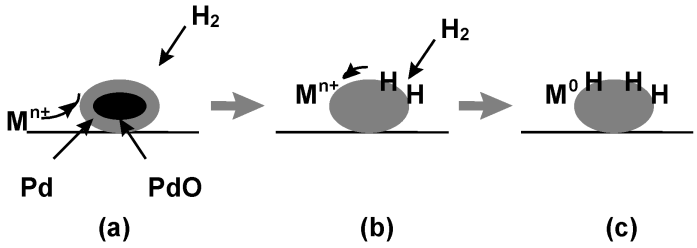

Table 6 Structural parameters obtained from the curve fitting of EXAFS data analysis of the EXAFS spectrum above the Pd K edge

Sample	*Pair*	*N*	*R* (nm)	σ^2 (pm^2)[a]
Pd/La-Al_2O_3	Pd-O	3.5	0.201	17
	Pd-Pd	4.8	0.305	58
	Pd-Pd	4.2	0.343	42
Pt/Pd/La-Al_2O_3	Pd-O	2.0	0.201	54
(Pt/Pd = 0.5)	Pd-Pd	2.7	0.271	56
	Pd-Pt	4.2	0.267	49
Pt/Pd/La-Al_2O_3	Pd-O	–	–	–
(Pt/Pd = 1.0)	Pd-Pd	5.2	0.273	57
	Pd-Pt	4.2	0.270	73
Pt/Pd/La-Al_2O_3	Pd-O	–	–	–
(Pt/Pd = 2.0)	Pd-Pd	2.3	0.273	63
	Pd-Pt	7.4	0.270	96

[a]The Debye-Waller factor.

Table 7 Structural parameters obtained from the curve fitting of XAFS spectrum above the Pt L_{III} edge

Sample	*Pair*	*N*	*R* (nm)	σ^2 (pm^2)[a]
Pt/Pd/La-Al_2O_3	Pt-O	3.4	0.193	142
(Pt/Pd = 0.5)	Pt-Pd	4.3	0.258	56
	Pt-Pt	4.7	0.259	49
Pt/Pd/La-Al_2O_3	Pt-O	1.3	0.201	82
(Pt/Pd = 1.0)	Pt-Pd	1.7	0.272	38
	Pt-Pt	3.4	0.271	70
Pt/Pd/La-Al_2O_3	Pt-O	1.3	0.199	58
(Pt/Pd = 2.0)	Pt-Pd	1.2	0.272	35
	Pt-Pt	5.1	0.271	70

[a]The Debye-Waller factor.

The bimetallic PtPd nanoparticle of Pt/Pd = 1.0 showed a little different change of XANES spectrum as a function of heating temperature in Figure 16. The metallic XANES features were retained over the temperature range upon heating and cooling except the slight change at around 973 K. The structure of the bimetallised Pd nanoparticle seems to remain the same. Thus, the inhibition of the reversible structural transformation of the bimetallic PtPd nanoparticles can be suggested based on the results of the measurement of XANES as a function of temperature. The summary of the reversible transformation is presented in Table 8.

Figure 16 Near edge spectra of the PtPd bimetallic nanoparticles measured as a function of heating temperatures at (a) the Pd *K* edge and (b) the Pt L_{III} edge

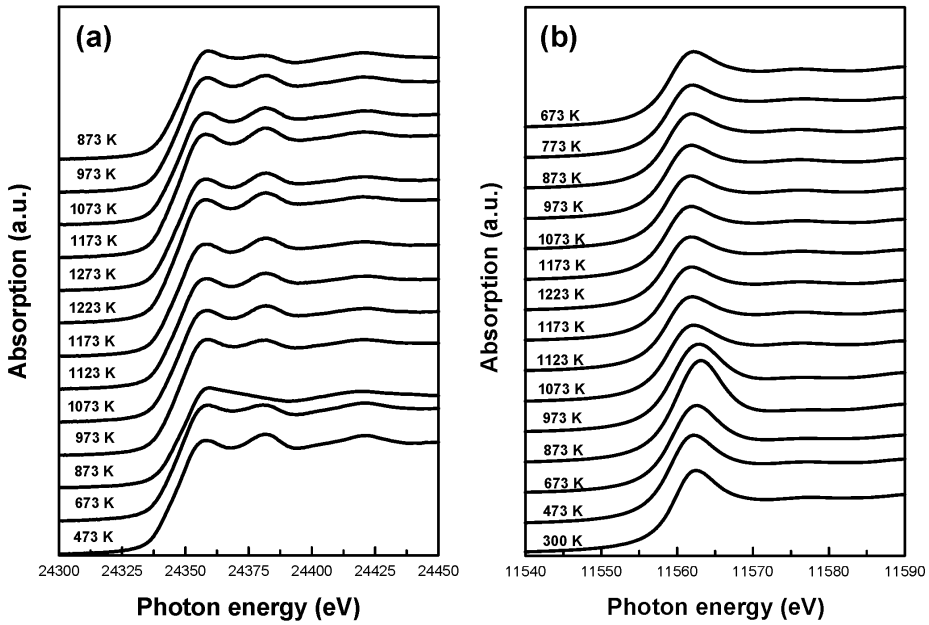

Table 8 Summary of the reversible transformation temperature obtained from the measurement of the XANES as a function of temperature

Sample	$T_{PdO \rightarrow Pd}$ (K)	$T_{Pd \rightarrow PdO}$ (K)
Pd/La-Al_2O_3	1123	950
TiO_2-Pd/La-Al_2O_3	1273	<973
ZrO_2-Pd/La-Al_2O_3	1273	<970
Pt/Pd/La-Al_2O_3	~973	<873

Figure 17 shows the catalytic activity of the methane combustion as a function of reaction temperature. The catalytic activity of Pd only catalyst had a strong catalytic hysteresis with 100 K temperature gap. The platinum catalyst also showed the weak hysteresis, which the catalytic performance was inferior to that of the Pd catalyst. However, the bimetallised Pd catalyst with Pt showed no hysteresis in the methane combustion. It seems to be due to the formation of platinum-enriched palladium nanoparticles as suggested from the results of XANES.

Figure 17 Catalytic activity of (circle) 2 wt% Pd/La-Al_2O_3, (rectangular) 2 wt% Pt/La-Al_2O_3, and (triangle) Pt/Pd/La-Al_2O_3 (Pt/Pd = 0.5). The open and closed symbols indicate the increase and the decrease of the reaction temperature, respectively

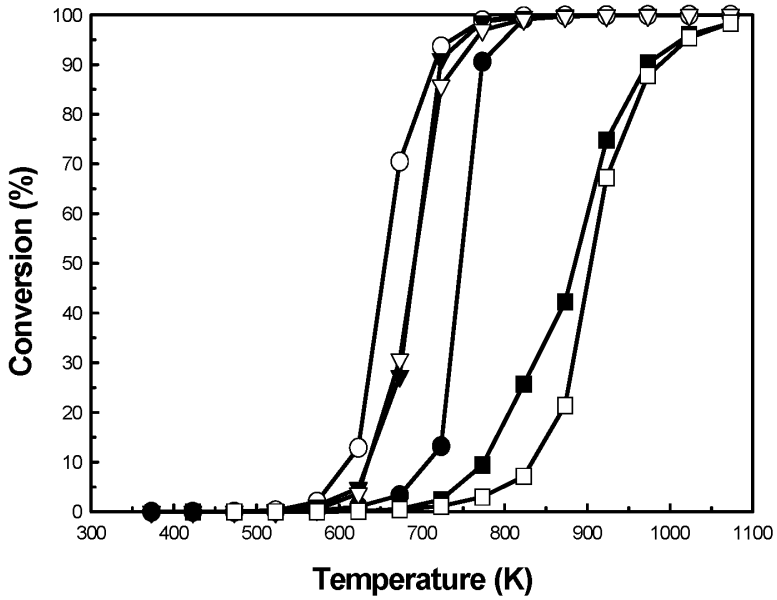

The bimetallisation of the Pd catalyst with Pt changed completely the reversible structural transformation by forming the platinum enriched palladium nanoparticles. The effect of the bimetallisation is the removal of catalytic hysteresis in methane combustion and the same catalytic entity over the temperature range, consistent with the results of XAFS/XANES.

4 Conclusion

The rational design of the bimetallic nanoparticles comprising of cherry type model in which the one specific metal was deposited preferentially on the other metal was achieved with the proper pretreatments after the formation of the nanoparticle and subsequently loading of the second component metal. Such microstructural control can be possible based on the information on the formation and growth of monometallic nanoparticles obtained through the combined studies of XAFS, xenon adsorption and ^{129}Xe NMR spectroscopy. The generated bimetallic nanoparticles showed the improved catalytic performance compared to that of monometallic nanoparticles. The reduction mechanism proposed in the review provides basic understanding about how the specific microstructure can be made using the conventional pretreatment method. Thereby the economical preparation technology for the bimetallic nanoparticles can be built employing the simple reduction mechanism as above-mentioned.

Acknowledgement

This work was supported by Korean Research Foundation Grant (KRF-2003-003-D00087). The author (S.J. Cho) acknowledged the generous permission to use the synchrotron radiation at the Pohang Accelerator Laboratory.

References

1 Gates, B.C. (1995) 'Supported metal clusters: synthesis, structure, and catalysis', *Chem. Rev*., Vol. 95, p.511.

2 Jacobs, P.A. (1986) *Metal Clusters in Catalysis*, *Stud. Surf. Sci. Catal.*, Vol. 29, pp.357.

3 Forger, K. (1984) 'Dispersed metal catalyst' in Anderson, J.R. and Boudart, M. (Eds.): *Catalysis Science and Technology*, Springer-Verlag, Berlin, Vol. 6, p.227.

4 Boudart, M. and Djega-Mariadassou, G. (1984) *Kinetics of Heterogeneous Catalytic Reactions*, Princeton University Press, p.20.

5 (a) Gellezot, P. (1979) 'The state and catalytic properties of platinum and palladium in Faujasite-type zeolie', *Catal. Rev. Sci. Eng*., Vol. 20, p.121; (b) Betta, R.A.D. and Boudart, M. (1973) in Hightower, J. (Ed.): *Proceedings of the 5th International Congress on Catalysis*, North Holland, Vol. 2, p.1329; (c) Chmelka, B.F., Ryoo, R., Liu, S-B., de Menorval, L.C., Radke, C.J., Patersen, E.E. and Pines, A. (1988) 'Probing metal cluster formation in NaY zeolite by xenon-129 NMR', *J. Am. Chem. Soc.*, Vol. 10, p.4465.

6 (a) Sinfelt, J.H. (1983) *Bimetallic Catalysts: Discoveries, Concepts and Applications*, John Wiley & Sons (b) Meitzner, G., Via, G.H., Lytle, F.W., Fung, S.C. and Sinfelt, J.H. (1988) 'Extended x-ray absorption fine structure (EXAFS) studies of platinum-tin catalysts', *J. Phys. Chem.*, Vol. 92, p.2925.

7 Ichikuni, N. and Iwasawa, Y. (1993) 'In situ d electron density of Pt particles on supports by XANES', *Catal. Lett*., Vol. 20, p.87.

8 Cho, S.J. and Kang, S.K. (2004) 'Structural transformation of PdPt nanoparticles probed with X-ray absorption near edge structure', *Catal. Today*, Vol. 93–95, p.561.

9 Chen, Q.J., Ito, T. and Fraissard, J. (1991) '^{129}Xe-NMR study of rare earth-exchanged Y zeolites', *Zeolites*, Vol. 11, p.239.

10 Gedeon, A., Bonardet, J.L., Ito, T. and Fraissard, J. (1989) 'Application of xenon-129 NMR to the study of Ni^{2+} Y zeolites', *J. Phys. Chem*., Vol. 93, p.2563.

11 Boudart, M., Ryoo, R., Valenca, G.P. and van Grieken, R. (1993) 'Chemisorption of H_2 on supported Pt clusters probed by^{129}Xe NMR', *Catal. Lett*., Vol. 17, p.273.

12 (a) Ryoo, R., Cho, S.J., Pak, C., Kim, J-G., Ihm, S-K. and Lee, J.Y. (1992) 'Application of the xenon-adsorption method for the study of metal cluster formation and growth on Y zeolite', *J. Am. Chem. Soc*., Vol. 114, p.76; (b) Ryoo, R., Cho, S.J., Pak, C. and Lee, J.Y. (1993) 'Clustering of platinum atoms into nanoscale particle and network on NaY zeolite', *Catal. Lett.*, Vol. 20, pp.107–115.

13 (a) Pak, C., Cho, S.J., Lee, J.Y. and Ryoo, R. (1994) 'Preparation of iridium clusters in Zeolite Y via Cation exchange: EXAFS, Xenon adsorption, and ^{129}Xe NMR studies', *J. Catal*., Vol. 149, p.61; (b) Yang, O.B., Woo, S.I. and Ryoo, R. (1992) 'Formation of small Pt-Ir bimetallic clusters in NaY zeolite probed with ^{129}Xe NMR spectroscopy and ethane hydrogenolysis', *J. Catal*., Vol. 137, p.357.

14 Beutel, T., Knözinger, H., Treviño, H., Zhang, Z.C., Sachtler, W.M.H., Dossi, C., Psaro, R. and Ugo, R. (1994) 'Manganese-promoted rhodium/NaY zeolite catalysts. An IR spectroscopic study', *J. Chem. Soc., Faraday Trans.*, Vol. 90, p.1335.

15 (a) Cho, S.J., Jung, S.M., Shul, Y.G. and Ryoo, R. (1992) 'Formation and growth of a ruthenium cluster in a Y zeolite supercage probed by xenon-129 NMR spectroscopy and xenon adsorption measurements', *J. Phys. Chem*., Vol. 96, p.9922; (b) Shoemaker, R. and Apple, T. (1987) 'Redox Behavior of Ruthenium in Zeolite Y', *J. Phys. Chem*., Vol. 91, p.4024.

16 Kim, J-G., Ihm, S-K., Lee, J.Y. and Ryoo, R. (1991) 'Formation of a small palladium cluster by anchoring on a multivalent cation in a zeolite supercage studied by xenon adsorption', *J. Phys. Chem*., Vol. 95, p.8546.

17 (a) Voorhoeve, R.J.H., Remeika, J.P. and Trimble, L.E. (1974) 'Perovskites containing ruthenium as catalysts for nitric oxide reduction', *Mater. Res. Bull.,* Vol. 9, p.1393; (b) Verdonck, J.J., Jacobs, D.A., Genet, M. and Poncelet, G. (1980) 'Redox behaviour of transition metal ions in zeolites. Part 8. – Characterization of a ruthenium metal phase in NaY zeolite', *J. Chem. Soc., Faraday Trans. 1*, Vol. 76, p.403.

18 (a) Crespin, M. and Hall, W.K. (1981) 'The surface chemistry of some perovskite oxides', *J. Catal.*, Vol. 69, p.359. (b) Crespin, M., Levitz, P. and Gatineau, L. (1983) 'Reduced forms of $LaNiO_3$ perovskite. Part 1–Evidence for new phases: $La_2Ni_2O_5$ and $LaNiO_2$', *J. C. S. Faraday II*, Vol. 79, p.1181.

19 Cho, S.J. (1997) 'Structure and reactivity of Pt cluster and Pt-based bimetallic cluster supported on KL zeolite', *PhD Thesis*, Korea Advanced Institute of Science and Technology, Chap. 4, p.104.

20 (a) Cho, S.J., Ahn, W.S., Hong, S.B. and Ryoo, R. (1996) 'Characterization of PtSn nanoparticles in KL zeolite and *n*-hexane aromatization activity', *J. Phys. Chem.*, Vol. 100, p.4996; (b) Cho, S.J. and Ryoo, R. (2004) *Catal. Lett.*, Vol. 97, Nos. 1–2, p.71.

21 (a) Koningsber, D.C. and Prins, R. (1988) *Principles, Application, Techniques of EXAFS, SEXAFS, and XANES*, Wiley; (b) Newville, M., Livins, P., Yacoby, Y., Rehr, J.J. and Stern, E.A. (1993) 'Near-edge x-ray-absorption fine structure of Pb: a comparison of theory and experiment', *Phys. Rev. B*, Vol. 47, p.14126; (c) Frenkel, A., Stern, E.A., Voronel, A., Qian, M. and Newville, M. (1994) 'Solving the structure of disordered mixed salts', *Phys. Rev. B*, Vol. 49, p.11662; (d) Stern, E.A. (1993) 'Number of relevant independent points in x-ray-absorption fine-structure spectra', *Phys. Rev. B*, Vol. 48, p.9825.

22 (a) Rehr, J.J., Albers, R.C. and Zabinsky, S.I. (1992) 'High-order multiple-scattering calculations of x-ray-absorption fine structure', *Phys. Rev. Lett*., Vol. 69, p.3397. (b) Ellis, P.J. and Freeman, H.C. (1995) 'XFIT – an interactive EXAFS analysis program', *J. Synchrotron Rad*., Vol. 2, p.190.

23 Schlatter, J.C. and Boudart, M. (1974) 'Hydrogenation of ethylene on supported platinum', *J. Catal.*, Vol. 24, p.482.

24 Srinivasan, R. and Davis, B.H. (1992) 'The structure of platinum-tin reforming catalysts', *Platinum Met. Rev.*, Vol. 36, p.119.

25 (a) Caballero, A., Dexpert, H., Didillon, B., LePeltier, F., Clause O. and Lynch, J. (1993) 'In situ x-ray absorption spectroscopic study of a highly dispersed platinum-tin/alumina catalyst', *J. Phys. Chem*., Vol. 97, p.11283; (b) Davis, B.H. (1993) 'Platinum-tin-alumina catalysts: relating characterization and alkane dehydrocyclization data', in Guczi, L. *et al.* (Eds.): *Studies in Surface Science and Catalysis*, Vol. 75, p.889.

26 Meriaudeau, P., Naccache, C., Thangaraj, A., Bianchi, C.L., Carli, R., Vishvanathan, V. and Narayanan, S. (1995) 'Studies on Pt_xSn_y bimetallics in NaY: I preparation and characterization', *J. Catal*., Vol. 154, p.345.

27 Xu, C., Tsai, Y.L. and Koel, B.E. (1994) 'Adsorption of cyclohexane and benzene on ordered tin/platinum (111) surface alloys', *J. Phys. Chem.*, Vol. 98, p.585.

28 Cortright, R.D. and Dumesic, J.A. (1995) 'L-zeolite-supported platinum and platinum/tin catalysts for isobutane dehydrogenation', *Appl. Catal. A: General*, Vol. 129, p.101.

29 (a) Ryoo, R., Pak, C. and Cho, S.J. (1993) 'EXAFS and catalytic activity of AgPt bimetallic cluster supported on NaY zeolite', *Jpn. J. Appl. Phy*s., Vol. 32-2, p.475; (b) Pak, C., and Ryoo, R. (1995) 'Application of ^{129}Xe NMR spectroscopy to probe the formation of a bimetallic cluster in zeolite', *Appl. Mag. Reson.*, Vol. 8, p.475.

30 Ahn, D.H., Lee, J.S., Nomura, M., Sachtler, W.M.H., Moretti, G., Woo, S.I. and Ryoo, R. (1992) 'Characterization of zeolite-supported Pt-Cu bimetallic catalyst by xenon-129 NMR and EXAFS', *J. Catal*., Vol. 133, p.191.

31 Coughlan, B. and Keane, M.A. (1991) 'The hydrogenation of benzene over nickel-supported Y zeolites. Part 2. A mechanistic approach', *Zeolites*, Vol. 11, p.483.

32 Coughlan, B. and Keane, M.A. (1992) 'Catalyst deactivation during the hydrogenation of benzene over nickel-loaded Y zeolites', *J. Mol. Catal*., Vol. 71, p.93.

33 (a) Che, M. and Bennet, C.O. (1989) 'The influence of particle size on the catalytic properties of supported metals', *Adv. Catal*., Vol. 36, p.55; (b) Zhao, A. and Gates, B.C. (1996) 'Hexairidium clusters supported on γ-Al_2O_3: synthesis, structure, and catalytic activity for toluene hydrogenation', *J. Am. Chem. Soc*., Vol. 118, p.2458.

34 Cho, S.J. And Kang, S.K. (2000) 'Reversible structural transformation of palladium catalyst supported on La-Al_2O_3 probed with X-ray absorption fine structure', *J. Phys. Chem. B*, Vol. 104, p.8124.

35 Rodriguez, N.M., Oh, S.G., Dalla Betta, R.A. and Baker, R.T.K. (1995) '*n*-Situ Electron Microscopy Studies of Palladium Supported on Al_2O_3 SiO_2, and ZrO_2 in Oxygen', *J. Catal*., Vol. 157, p.676.

36 Asakuara, K., Inukai, J. and Iwasawa, Y. (1992) 'Structure of one atomic layer titanium oxide on silica and its palladium-mediated restructuring', *J. Phys. Chem.*, Vol. 96, p.829.